

# Three-dimensional lattice modulations in the charge density wave system $\text{Lu}_2\text{Ir}_3\text{Si}_5$


V. Petkov<sup>1,\*</sup>, A. Zafar<sup>1</sup>, M. Jakhar<sup>1,2</sup>, AM Milinda Abeykoon,<sup>3</sup> and Z. Hegedüs<sup>4</sup>

<sup>1</sup>*Department of Physics, Central Michigan University, Mt. Pleasant, Michigan 48858, USA*

<sup>2</sup>*Inter-University Accelerator Center, Aruna Asaf Ali Marg, New Delhi, India*

<sup>3</sup>*Photon Sciences Division, Brookhaven National Laboratory, Upton, New York 11973, USA*

<sup>4</sup>*Photon Science, Deutsches Elektronen-Synchrotron DESY, 22607 Hamburg, Germany*

 (Received 25 August 2025; revised 8 October 2025; accepted 27 October 2025; published 4 December 2025)

Using total and resonant x-ray scattering coupled to large-scale computer modeling, we study the lattice modulations in the complex charge density wave (CDW) material  $\text{Lu}_2\text{Ir}_3\text{Si}_5$ . We find that it is a unique quantum system where periodic lattice modulations related to emergent CDW order occur in three orthogonal atomic planes of the crystal lattice, leading to the emergence of an unusual three-dimensional (3D) pattern of short and long Ir-Ir and Lu-Lu bonds. The 3D character of observed lattice modulations explains the largely isotropic character of the changes in the electronic properties occurring when the CDW order sets in, demonstrating the strong electron-lattice coupling in  $\text{Lu}_2\text{Ir}_3\text{Si}_5$ . The result is supported by DFT calculations based on the experimental structure data. Altogether, our work provides strong evidence for the presence of a relationship between the dimensionality of emergent lattice distortions and that of concurrent changes in the electronic properties of CDW materials. The relationship may need to be accounted for when these materials are explored for practical applications.

DOI: [10.1103/PhysRevB.112.224108](https://doi.org/10.1103/PhysRevB.112.224108)

## I. INTRODUCTION

The interaction between spin, orbital, charge, and lattice degrees of freedom in quantum systems leads to the emergence of unusual collective electronic states such as charge density waves (CDWs) [1–3]. In low-dimensional systems, CDWs and associated lattice distortions are believed to be due to Fermi surface (FS) nesting effects paired with electron-lattice interactions [4–6]. In three-dimensional (3D) systems, the origin of CDWs is still under debate, ranging between a weak-coupling mechanism driven by electronic states near the Fermi level and a strong-coupling scenario envisaging prevalent electron-electron and electron-lattice interactions [7–10]. This renders CDW phenomena a contemporary topic in quantum materials research.

Rare-earth silicides  $\text{RE}_2\text{Ir}_3\text{Si}_5$  ( $\text{RE} = \text{Y, La, Ce-Nd, Gd-Lu}$ ) are complex materials exhibiting intertwined superconducting, magnetic, and CDW orders [11–14]. In this series, the end member  $\text{Lu}_2\text{Ir}_3\text{Si}_5$  is of special interest, as it exhibits superconductivity at 3.5 K and a first-order CDW transition at  $T_{\text{CDW}}$  of about 150 K and 200 K upon cooling and warming the material, respectively. The transition is accompanied by large anomalies in the resistivity, heat capacity, and magnetic susceptibility [15–18]. At room temperature, the material adopts an orthorhombic space group (S.G.) *Ibam* type structure where zigzag chains of Ir atoms running in parallel to the *c* axis of the crystal lattice are separated by planes of Lu atoms, as shown in Figs. 1(a) and 1(b) and Fig. S1 [19]. Recent studies have suggested that the CDW order emerged below 200 K is incommensurate in character and

accompanied by a unique orthorhombic-to-triclinic lattice distortion involving Ir atoms [20]. However, other studies have suggested that the CDW order involves correlated displacements of Lu atoms from their average room-temperature positions. It has also been suggested that the CDW state is essentially phase segregated, where the volume ratio of the CDW and non-CDW phases changes with temperature [15]. Using total and resonant x-ray scattering coupled to large-scale structure modeling, we show that  $\text{Lu}_2\text{Ir}_3\text{Si}_5$  is single phase below  $T_{\text{CDW}}$ , where strong electron-lattice interactions make a key contribution to the emergence of CDWs. Moreover, the material is a rare example of a quantum system where periodic lattice modulations related to emergent CDW order include distortion modes occurring in three orthogonal atomic planes.

## II. RESULTS AND DISCUSSION

A polycrystalline  $\text{Lu}_2\text{Ir}_3\text{Si}_5$  sample was prepared by arc melting in argon atmosphere. The arc-melted sample was further annealed at 900 °C for 12 days, as sealed in a quartz tube. In-house x-ray diffraction (XRD) experiments showed that the resulting material is single phase at room temperature. Magnetic data taken as a function of temperature show a pronounced hysteresis effect, which is to be expected for a first-order phase transition (Fig. S2 [19]).

Total x-ray scattering experiments were carried out at the 28-ID-1 beamline at the National Synchrotron Light Source-II, Brookhaven National Laboratory, using x-rays with energy of 74.46 keV. The sample was positioned inside a liquid He cryostat used to control its temperature. Scattered x-ray intensities were collected while decreasing temperature from 300 K to 60 K in steps of 5 K using a PerkinElmer area detector. Total

\*Contact author: petko1vg@cmich.edu

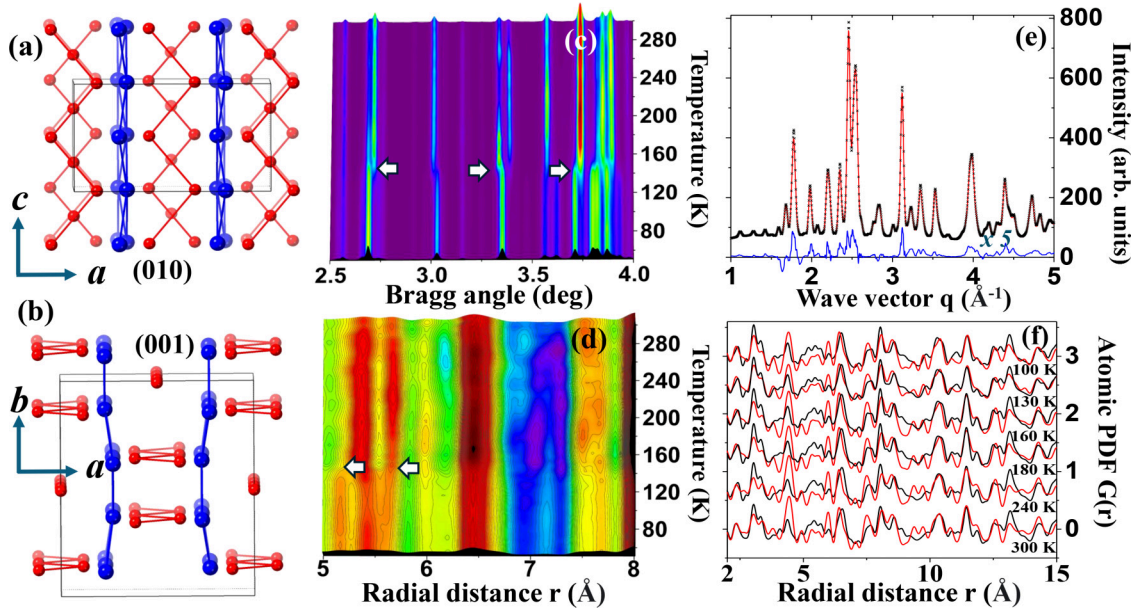


FIG. 1. Projection of the room-temperature structure for  $\text{Lu}_2\text{Ir}_3\text{Si}_5$  down the (a)  $y$  and (b)  $z$  axis of the orthorhombic lattice as determined by prior single-crystal studies. The structure features zigzag chains of Ir atom (red) sandwiched between planes of Lu (blue) atoms. Silicon atoms are not shown for clarity. (c) XRD and (d) total PDF intensity-colored maps. The data are obtained upon cooling the material. Arrows in (c) highlight a sharp shift in the position of XRD peaks taking place at  $T_{\text{CDW}}$  of about 150 K. Arrows in (d) highlight the emergence of an extra PDF peak, i.e., interatomic distances, at 5.2 Å and merging of the PDF peaks at 5.4 Å and 5.6 Å upon cooling the material to about 150 K. The intensity in (c), (d) increases linearly as the color changes from blue to red. (e) XRD patterns for  $\text{Lu}_2\text{Ir}_3\text{Si}_5$  taken at 35 eV (red) and 500 eV (black) below the K edge of Ir. Their difference (times a factor of 5) is also shown (blue). (f) Representative total (black) and Ir-differential (red) PDFs obtained at different temperatures.

atomic pair distribution functions (PDFs) were obtained from the experimental XRD patterns using standard procedures [21]. Intensity-colored maps for the patterns and respective total PDFs are shown in Figs. 1(c) and 1(d). Sharp changes in XRD and PDF peaks are clearly seen to take place at  $T_{\text{CDW}}$  of about 150 K, confirming the presence of a first-order phase transition. As obtained, however, total PDFs reflect six distinct pair correlations between Lu, Ir, and Si atoms in  $\text{Lu}_2\text{Ir}_3\text{Si}_5$  [22,23], that is, Lu-Lu, Lu-Ir, Lu-Si, Ir-Ir, Ir-Si, and Si-Si pair correlations. The correlations overlap heavily [Fig. 2(a)], making it difficult to interpret the total PDFs for  $\text{Lu}_2\text{Ir}_3\text{Si}_5$  unambiguously. To obtain structure data with increased sensitivity to atomic correlations involving Ir atoms, which are suggested to participate in the lattice modulations accompanying the CDW order [20], we carried out a resonant x-ray scattering experiment [24,25] at the K edge of Ir species (76.111 keV). Data were taken at several temperatures between 100 K and 300 K, where the temperature was controlled by a cryocooler device. Resonant data were collected at the beamline P21.2 [26] of the Deutsches Elektronen-Synchrotron using a PilatusX CdTe detector. At each temperature point, two XRD patterns were collected using x-rays with energy that is 35 eV and 500 eV below the K edge of Ir, respectively. From the intensity difference between the two patterns [Fig. 1(e)], Ir-differential PDFs were derived following a protocol described in Refs. [25,27]. As obtained, Ir-differential PDFs reflect only correlations involving Ir atoms, that is, Ir-Ir, Ir-Lu, and Ir-Si pair correlations [see Fig. 2(b)], which renders them significantly different from the respective total PDFs [Figs. 1(f) and 2(c)]. Hence, they provide an extra

Ir-species-specific experimental constraint for the structure modeling described below. More experimental details can be found in the Supplemental Material [19].

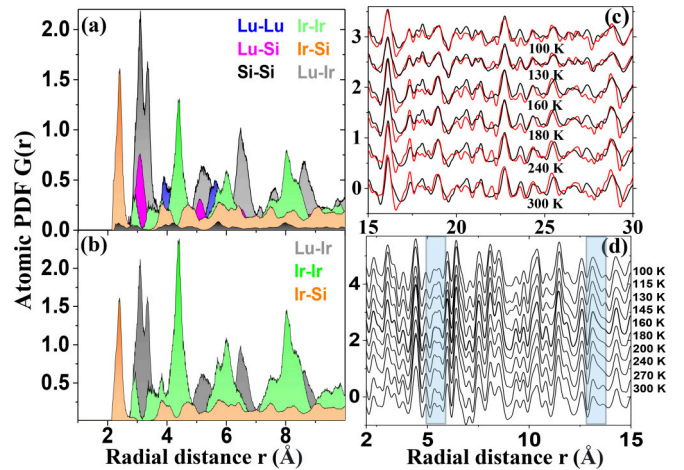


FIG. 2. (a) Computed partial atomic correlations contributing to the (a) total and (b) Ir-differential PDF for  $\text{Lu}_2\text{Ir}_3\text{Si}_5$ . Note that Ir-Ir correlations (green) heavily overlap with Lu-Lu, Lu-Si, and Si-Si correlations in the total PDF data, which is not the case with the Ir-differential PDFs. (c) Comparison between higher- $r$  parts of experimental total and Ir-differential PDFs revealing their significant difference. (d) Expanded view of the low- $r$  part of Ir-differential PDFs obtained at different temperatures. Light-blue shaded rectangles highlight systematic changes in the Ir-differential PDFs, i.e., Ir involving interatomic distances, with temperature.

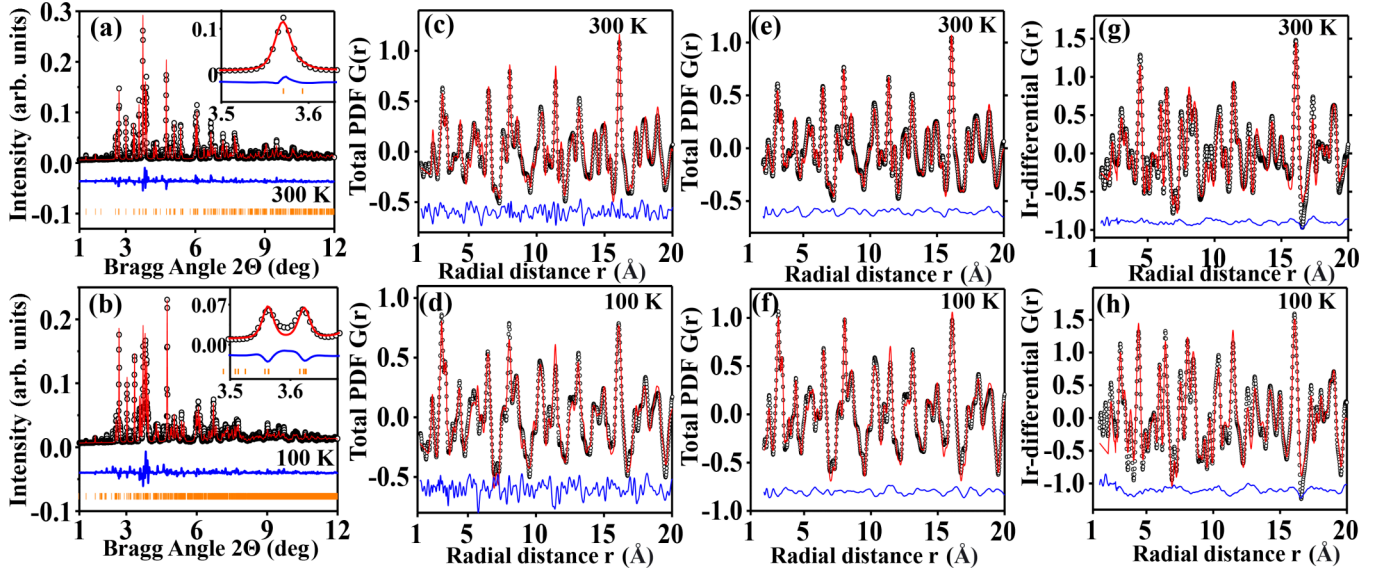


FIG. 3. (a), (b) Rietveld fits (red) to XRD patterns (symbols) for  $\text{Lu}_2\text{Ir}_3\text{Si}_5$  obtained at 300 K and 100 K. Vertical orange bars indicate positions of Bragg peaks. Fits to Bragg peaks strongly evolving with temperature are shown in the insets. The goodness-of-fit factor is about 8% for the 300-K fit and 10% for the 100-K fit. (c), (d) Crystallographic unit-cell-based fits (red) to total PDFs (symbols) for  $\text{Lu}_2\text{Ir}_3\text{Si}_5$  obtained at 300 and 100 K. The goodness-of-fit factor is about 18%. RMC fits (red) to (e) total and (g) Ir-differential PDFs (symbols) obtained at 300 K. RMC fits (red) to (f) total and (h) Ir-differential PDFs (symbols) obtained at 100 K. The goodness-of-fit factor for the RMC fits to total PDFs is about 5% and that to Ir-differential PDFs is about 7%. For all fits, the residual difference (blue) is shifted for clarity.

The temperature evolution of the average crystal structure for  $\text{Lu}_2\text{Ir}_3\text{Si}_5$  was assessed by Rietveld analysis of the experimental XRD data using the software GSAS-II [28]. The data collected at temperatures above 150 K were fit with an orthorhombic S.G. *Ibam*-type model. The model successfully reproduced the experimental data, as illustrated by the representative Rietveld fit shown in Fig. 3(a). The data collected at temperatures below 150 K were fit with a triclinically distorted (S.G.  $P\bar{1}$ ) version of the orthorhombic S.G. *Ibam*-type model suggested in Ref. [20], which has also been used to describe the CDW order in  $\text{Er}_2\text{Ir}_3\text{Si}_5$  and  $\text{Ho}_2\text{Ir}_3\text{Si}_5$  [12,14]. As illustrated by the representative Rietveld fit in Fig. 3(b), the model performed well, confirming the reduced average crystallographic symmetry of the CDW phase of  $\text{Lu}_2\text{Ir}_3\text{Si}_5$  in comparison to the room-temperature phase. The Rietveld refined lattice parameters and unit-cell volume are shown in Fig. 4. As can be seen in the figure, they sharply change at  $T_{\text{CDW}} \sim 150$  K.

The temperature evolution of the local structure for  $\text{Lu}_2\text{Ir}_3\text{Si}_5$  was assessed by PDF analysis, where PDFs obtained above and below  $T_{\text{CDW}}$  were approached with the S.G. *Ibam* and S.G.  $P\bar{1}$  model, respectively. The advantage of PDF analysis is that it takes into account both the Bragg and diffuse scattering components of the diffraction data, rendering it more sensitive to lattice distortions in comparison to Rietveld analysis. The computations were done using the software PDFGUI [29]. Representative fits are shown in Figs. 3(c) and 3(d), respectively. The orthorhombic model successfully fits the PDF obtained above  $T_{\text{CDW}}$ , confirming the absence of local lattice distortions in room-temperature  $\text{Lu}_2\text{Ir}_3\text{Si}_5$ . The triclinic model, however, appeared less successful in reproducing the PDFs obtained below  $T_{\text{CDW}}$ , indicating that the lattice distortions in the CDW phase of  $\text{Lu}_2\text{Ir}_3\text{Si}_5$  are more

complex than suggested previously. PDF refined lattice parameters and unit-cell volume are summarized in Fig. 4. A noticeable difference from the Rietveld results is that, locally,  $\text{Lu}_2\text{Ir}_3\text{Si}_5$  appears more compressed, i.e., with a reduced unit-cell volume, in comparison to the bulk state.

To assess the CDW ground-state structure for  $\text{Lu}_2\text{Ir}_3\text{Si}_5$  more precisely, we refined large-scale models against the experimental total PDF and Ir differential models obtained at 100 K using the reverse Monte Carlo (RMC) technique [30–32]. The

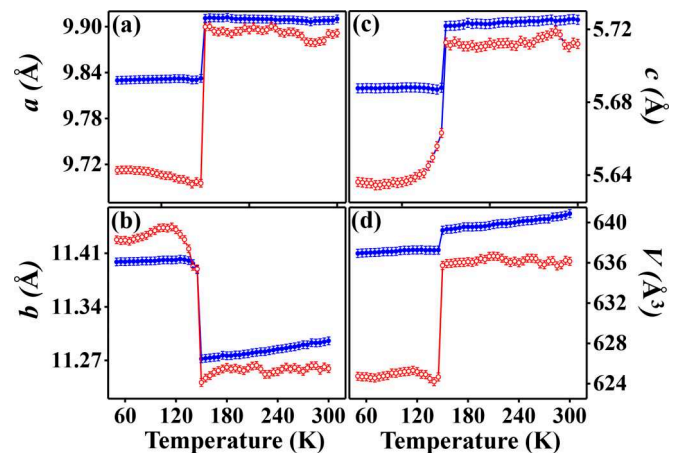


FIG. 4. Temperature evolution of the  $a$ ,  $b$ , and  $c$  lattice parameters and unit-cell volume  $V$  obtained by Rietveld (blue symbols) and small-scale PDF (red symbols) fits. Note that, as found in many complex materials [42–45], Rietveld and PDF refined structure parameters differ significantly due to the presence of local lattice distortions. The parameters and volume sharply change at  $T_{\text{CDW}} \sim 150$  K.



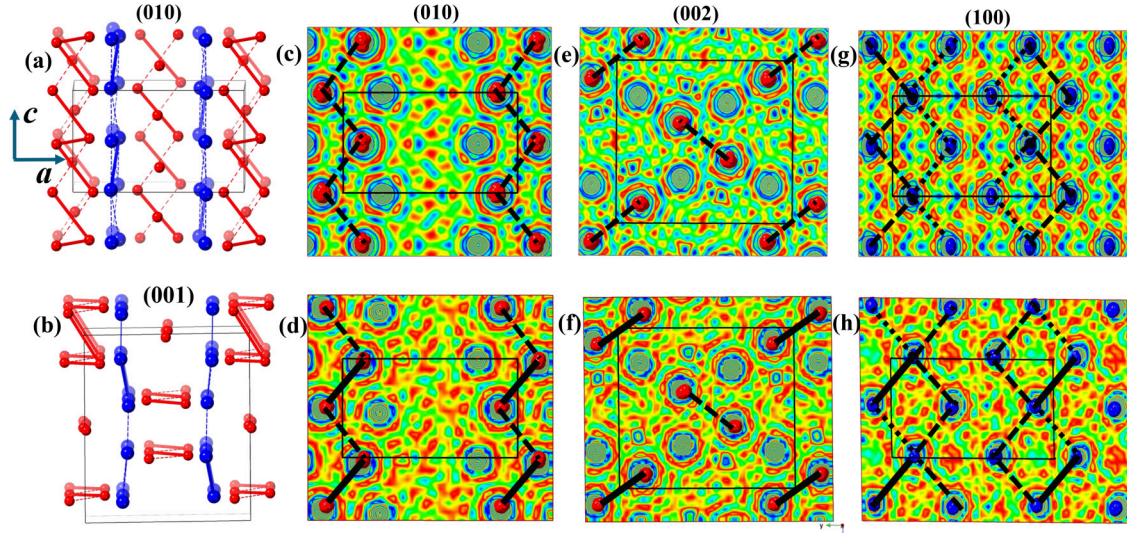


FIG. 5. Average atomic positions in the CDW (100-K) phase of  $\text{Lu}_2\text{Ir}_3\text{Si}_5$  seen down the (a)  $y$  and (b)  $z$  axis of the triclinic lattice as derived from large-scale RMC modeling. The structure features zigzag chains of Ir atoms comprising short (thick red line) and long (broken red line) Ir-Ir distances (red). The chains are sandwiched between distorted planes of Lu atoms exhibiting short (thick blue line) and long (broken blue line) Lu-Lu bonds. Silicon atoms are not shown for clarity. A commensurate approximation to the unit cell of the CDW phase  $\text{Lu}_2\text{Ir}_3\text{Si}_5$  is also shown (thin solid lines). It has been used to compute the electronic properties shown in Figs. 6(b) and 6(d). Projection of the electron density distribution for the (c) room-temperature and (d) CDW phases of  $\text{Lu}_2\text{Ir}_3\text{Si}_5$  onto the (010) plane where Ir atoms are shown as black circles. All Ir-Ir distances (broken line) have the same length of  $3.65 \text{ \AA}$  at room temperature. Short ( $\sim 3.4 \text{ \AA}$ ; solid black line) and long ( $\sim 3.7 \text{ \AA}$ ; broken line) Ir-Ir distances appear in the CDW phase. Projection of the electron density distribution for the (e) room-temperature and (f) CDW phases of  $\text{Lu}_2\text{Ir}_3\text{Si}_5$  onto the (002) plane Ir atoms are shown as black circles. All Ir-Ir distances (broken line) have the same length of  $3.9 \text{ \AA}$  at room temperature. Short ( $\sim 3.6 \text{ \AA}$ ; thick solid line) and long ( $\sim 3.9 \text{ \AA}$ ; broken line) Ir-Ir distances appear in the CDW phase. Projection of the electron density distribution for the (g) room-temperature and (h) CDW phases of  $\text{Lu}_2\text{Ir}_3\text{Si}_5$  onto the (100) plane where Lu atoms are shown as black circles. At room temperature, the plane exhibits short ( $4.0 \text{ \AA}$ ; dotted line) and somewhat longer ( $4.1 \text{ \AA}$ ; broken line) Lu-Lu distances. In the CDW phase, the plane exhibits a complex pattern of short ( $\sim 3.8 \text{ \AA}$ ; thick solid line), intermediate length ( $\sim 4.0 \text{ \AA}$ ; dotted line), and long ( $\sim 4.2 \text{ \AA}$ ; broken line) Lu-Lu distances. In all plots the unit cell is outlined with a thin gray line. The electron density increases as the color changes linearly from blue to red. The positions for Ir and Lu atoms in (a)–(f) appear as an average of 896 atomic positions of respective atoms in the 36 000-atom RMC models. As can be seen in the figure, the emergence of lattice modulations is accompanied by a redistribution of the electron density, indicating the presence of strong electron-lattice interactions.

model featured  $80 \text{ \AA} \times 90 \text{ \AA} \times 80 \text{ \AA}$  configurations of 36 000 Lu, Ir, and Si atoms in due proportions. The large model size allowed us to probe a statistically representative variety of distinct lattice distortions extending well beyond one crystallographic unit cell without applying strict crystallographic constraints that impose a particular lattice distortion pattern. For consistency, RMC fits to total and Ir-differential PDFs obtained at 300 K were also performed. Modeling details are given as Supplemental Material [19]. The success of the fits is demonstrated in Figs. 3(e)–3(h). An RMC-refined structure model for the CDW phase of  $\text{Lu}_2\text{Ir}_3\text{Si}_5$  is shown in Figs. 5(a) and 5(b). Projections of the electron density distribution in  $\text{Lu}_2\text{Ir}_3\text{Si}_5$  at 100 K and 300 K onto different atomic planes are shown in Figs. 5(c)–5(h), as derived from the respective RMC-refined models.

Comparison between the unit cells for  $\text{Lu}_2\text{Ir}_3\text{Si}_5$  above [Figs. 1(a) and 1(b)] and below [Figs. 5(a) and 5(b)]  $T_{\text{CDW}}$  reveals the presence of significant lattice distortions in the CDW phase. In particular, in line with the results of Ramakrishnan *et al.* [20], we find that both Ir and Lu atoms undergo correlated atomic displacements from their room temperature positions below  $T_{\text{CDW}}$ . Furthermore, in line with the results of S. Ramakrishnan *et al.* [20], we find that the displacements of Ir atoms lead to the emergence of short and long Ir-Ir

distances in the chains running in parallel to the  $c$  axis of the crystal lattice. The distances form a zigzag pattern in (010) atomic planes [Fig. 5(c) vs Fig. 5(d)]. In addition, we find that short and long Ir-Ir distances also emerge between adjacent Ir chains [Fig. 5(e) vs Fig. 5(f)]. The distances alternate in (002) atomic planes as shown in Fig. 5(f). Moreover, we notice an unusual pattern of short and long Lu-Lu distances in the planes of Lu atoms [(001) atomic planes] positioned between the Ir chains [Fig. 5(g) vs Fig. 5(h)]. Altogether, lattice modulations involving either Ir or Lu atoms appear in three orthogonal lattice planes below  $T_{\text{CDW}}$ , rendering the CDW in  $\text{Lu}_2\text{Ir}_3\text{Si}_5$  three-dimensional in character. It has been assumed but never proven that, largely, emerged lattice distortions paired with strong electron-lattice interactions and not changes in the geometry of FS are behind the changes in the electronic properties of  $\text{Lu}_2\text{Ir}_3\text{Si}_5$  below  $T_{\text{CDW}}$ . To verify the assumption, we conducted density functional theory (DFT) calculations, the details of which are given in the Supplemental Material [19]. The electronic band structure for  $\text{Lu}_2\text{Ir}_3\text{Si}_5$  at 300 K and 100 K is shown in Figs. 6(a) and 6(b), as computed from the RMC-refined structure models shown in Figs. 5(c), 5(e), and 5(g), and Figs. 5(d), 5(f), and 5(h) that exhibit and do not exhibit lattice distortions, respectively. The respective total density of states (DOS) near the Fermi energy

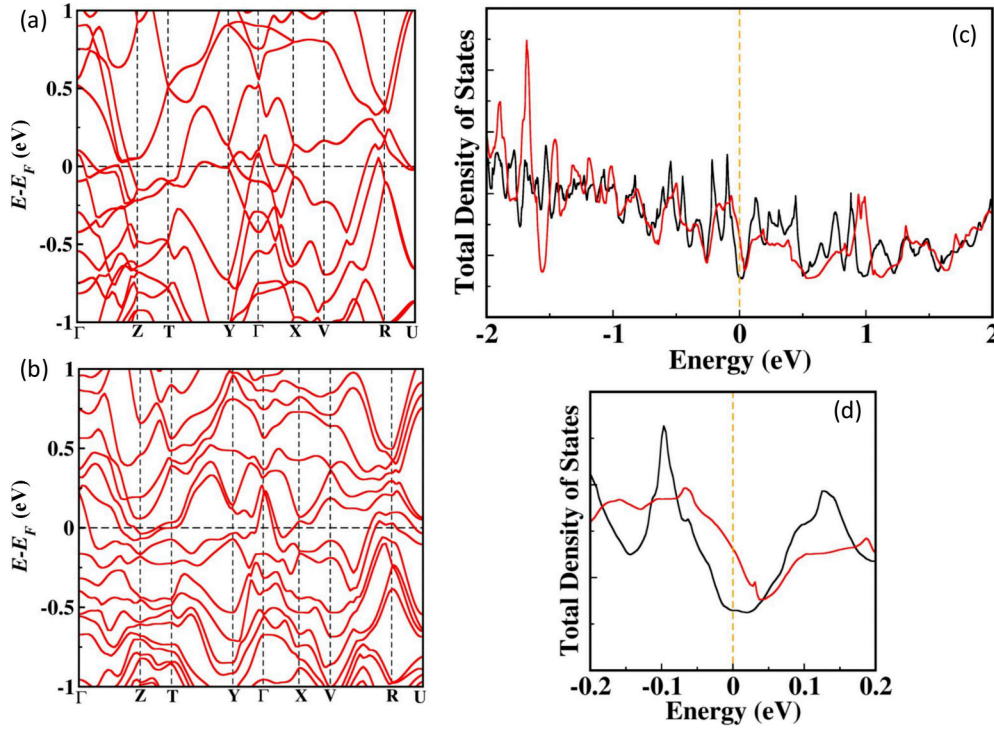


FIG. 6. Electronic band structure for  $\text{Lu}_2\text{Ir}_3\text{Si}_5$  at (a) 300 K and (b) 100 K, as computed from RMC-refined models shown in Figs. 5(c), 5(e), and 5(g) and 5(d), 5(f), and 5(h), respectively. (c) Total density of states (DOS) at 300 K (red line) and 100 K (black line). The Fermi energy ( $E_f$ ) is given with a vertical broken line. DOS at  $E_f$  is seen to decrease below  $T_{\text{CDW}}$  significantly but remains nonzero, which is consistent with the strongly reduced, yet metallic conductivity of the CDW phase of  $\text{Lu}_2\text{Ir}_3\text{Si}_5$ . Note that the difference between the atomic configurations used to compute the DOS at 300 K and 100 K is the absence [Figs. 5(c), 5(e), and 5(g)] and presence [Figs. 5(d), 5(f), and 5(h)] of lattice distortions, respectively. Therefore, the reduced DOS at  $E_f$  at 100 K in comparison to 300 K may be attributed to the emergence of lattice distortions and related charge density redistribution below  $T_{\text{CDW}}$ .

are shown in Figs. 6(c) and 6(d). As can be seen in the figure, the total DOS decreases below  $T_{\text{CDW}}$ . The decrease can be attributed to the emerged lattice distortion modes, providing strong evidence for the presence of strong electron-lattice interactions in  $\text{Lu}_2\text{Ir}_3\text{Si}_5$ . The decrease may well explain the observed drop in its electrical conductivity at  $T_{\text{CDW}}$  upon cooling the material [13,18].

Previous studies have shown that CDW systems where the lattice distortions emerging below  $T_{\text{CDW}}$  are anisotropic also exhibit anisotropic changes in their electronic properties. Examples include  $\text{NbSe}_3$  [33],  $2\text{H-NbSe}_2$  and  $2\text{H-TaSe}_2$  [34],  $\text{RETe}_3$  ( $\text{RE} = \text{La to Dy}$ ) [35],  $\text{AV}_3\text{Sb}_5$  ( $\text{A} = \text{K, Sb, Cs}$ ) [36],  $1\text{T-TaS}_2$  [37–39],  $\text{RENiC}_2$  ( $\text{RE} = \text{Sm, Gd, Tb, Dy}$ ) [40], and  $\text{LaPt}_2\text{Si}_2$  [41] systems. Interestingly, the significant changes in the electronic properties for  $\text{Lu}_2\text{Ir}_3\text{Si}_5$  taking place at  $T_{\text{CDW}}$  have been found to be comparable along the  $a$ ,  $b$ , and  $c$  axis of the crystal lattice, i.e., near isotropic [16]. Evidently, not only the electron-lattice interactions in  $\text{Lu}_2\text{Ir}_3\text{Si}_5$  are strong, but also the dimensionality of the emerged lattice distortions and that of the concurrent changes in the electronic properties the material experiences below  $T_{\text{CDW}}$  are strongly coupled.

### III. CONCLUSIONS

In summary, in line with results from prior studies, we find that  $\text{Lu}_2\text{Ir}_3\text{Si}_5$  suffers strong lattice distortions leading

to a collapse of the average crystallographic symmetry from orthorhombic to triclinic when CDW order sets in. The distortions involve correlated displacements of both Lu and Ir atoms from their room-temperature positions in the crystal lattice, leading to the emergence of ordered patterns of either Ir-Ir or Lu-Lu short and long bonds lying in three orthogonal atomic planes. Concurrently, the electronic properties undergo strong isotropic changes due to strong electron-lattice interactions. Yet, the material remains single phase, which can be described in terms of a unique structure model. The observed relationship between the dimensionality of emerged lattice distortions and that of concurrent changes in electronic properties is likely to be relevant to other members of the large 2-3-5 rare earth-iridium-silicide family and 3D CDW systems generally. Therefore, it may need to be accounted for when the systems are explored for practical applications. The advanced experimental approach employed here, which includes experiments sensitive to the arrangement of atomic species participating in the CDW lattice distortions, such as resonant x-ray scattering, coupled to large-scale structure modeling, can reveal any type of distinct distortion modes, and hence, facilitate that exploration.

### ACKNOWLEDGMENTS

This work was supported by the U.S. Department of Energy, Office of Science, Office of Basic Energy Sciences under

Award No. DE-SC0021973 and used resources of the National Synchrotron Light Source at the Brookhaven National Laboratory provided by the DOE Office of Science under Contract No. DE-SC0012704. We also acknowledge DESY (Hamburg, Germany), a member of the Helmholtz Association HGF, for the provision of experimental facilities. PARAM Rudra, a national supercomputing facility, at Inter-University Accelerator Centre (IUAC), New Delhi, has been used to obtain the DFT

results presented in this paper. Thanks are due to C. Chavez for the help with synchrotron experiments.

### DATA AVAILABILITY

High-resolution XRD data shown in Fig. 1 are available at [52] while other data are available from the authors upon reasonable request.

- [1] E. Fradkin, S. A. Kivelson, and J. M. Tranquada, *Colloquium: Theory of intertwined orders in high temperature superconductors*, *Rev. Mod. Phys.* **87**, 457 (2015).
- [2] Z. Wang and S. C. Zhang, Chiral anomaly, charge density waves, and axion strings from Weyl semimetals, *Phys. Rev. B* **87**, 161107 (2013).
- [3] J. Gooth, B. Bradlyn, S. Honnali, C. Schindler, N. Kumar, J. Noky, Y. Qi, C. Shekhar, Y. Sun, Z. Wang, B. A. Bernevig, and C. Felser, Axionic charge-density wave in the Weyl semimetal  $(\text{TaSe}_4)_2\text{I}$ , *Nature (London)* **575**, 315 (2019).
- [4] M. D. Johannes and I. I. Mazin, Fermi surface nesting and the origin of charge density waves in metals, *Phys. Rev. B* **77**, 165135 (2008).
- [5] H. Fröhlich, On the theory of superconductivity: The one-dimensional case, *Proc. R. Soc. London Ser. A* **223**, 296 (1954).
- [6] R. E. Peierls, *Quantum Theory of Solids* (Oxford University Press, London, 1955).
- [7] T. M. Rice and G. K. Scott, New mechanism for a charge-density-wave instability, *Phys. Rev. Lett.* **35**, 120 (1975).
- [8] C. M. Varma and A. L. Simons, Strong-coupling theory of charge-density-wave transitions, *Phys. Rev. Lett.* **51**, 138 (1983).
- [9] H. Li, T. T. Zhang, T. Yilmaz, Y. Y. Pai, C. E. Marvinney, A. Said, Q. W. Win, C. S. Gong, Z. J. Tu, E. Vescovo, C. S. Nelson, R. G. Moore, S. Murakami, H. C. Lei, B. J. Lawrie, and H. Miao, Observation of unconventional charge density wave without acoustic phonon anomaly in kagome superconductors  $\text{AV}_3\text{Sb}_5$  ( $A = \text{Rb}, \text{Cs}$ ), *Phys. Rev. X* **11**, 031050 (2021).
- [10] R. Comin, A. Frano, M. M. Yee, Y. Yoshida, H. Eisaki, E. Schierle, E. Weschke, R. Sutarto, F. He, A. Soumyanarayanan, Y. He, M. LE Tacon, I. S. Elfimov, J. E. Hoffman, G. A. Sawatzky, B. Keimer, and A. Damascelli, Charge order driven by Fermi-arc instability in  $\text{Bi}_2\text{Sr}_{2-x}\text{La}_x\text{CuO}_{6+\delta}$ , *Science* **343**, 390 (2014).
- [11] C. Mazumdar, R. Nagarajan K. Ghosh, S. Ramakrishnan, B. D. Padalia, and L. C. Gupta, Low-temperature heat-capacity studies of  $\text{R}_2\text{Ni}_3\text{Si}_5$  ( $R = \text{Pr}, \text{Nd}, \text{Sm}, \text{Gd}, \text{Tb}, \text{Dy}, \text{Ho}$ ), *Phys. Rev. B* **59**, 4215 (1999).
- [12] S. Ramakrishnan, A. Schönleber, T. Rekiş, N. van Well, L. Noohinejad, S. van Smaalen, M. Tolkiehn, C. Paulmann, B. Bag, A. Thamizhavel, D. Pal, and S. Ramakrishnan, Unusual charge density wave transition and absence of magnetic ordering in  $\text{Er}_2\text{Ir}_3\text{Si}_5$ , *Phys. Rev. B* **101**, 060101(R) (2020).
- [13] Y. Singh, D. Pal, and S. Ramakrishnan, Low-temperature studies of the magnetic and superconducting properties of the  $\text{R}_2\text{Ir}_3\text{Si}_5$  ( $R = \text{Y}, \text{La}, \text{Ce}, \text{Nd}, \text{Gd}, \text{Tm}$ ) system, *Phys. Rev. B* **70**, 064403 (2004).
- [14] S. Ramakrishnan, J. Bao, C. Eisele, B. Patra, M. Nohara, B. Bag, L. Noohinejad, M. Tolkiehn, C. Paulmann, A. M. Schaller, T. Rekiş, S. R. Kotla, A. Schönleber, A. Thamizhavel, B. Singh, S. Ramakrishnan, and S. van Smaalen, Coupling between charge density wave ordering and magnetism in  $\text{Ho}_2\text{Ir}_3\text{Si}_5$ , *Chem. Mater.* **35**, 1980 (2023).
- [15] M. H. Lee, C. H. Chen, M.-W. Chu, C. S. Lue, and Y. K. Kuo, Electronically phase-separated charge-density waves in  $\text{Lu}_2\text{Ir}_3\text{Si}_5$ , *Phys. Rev. B* **83**, 155121 (2011).
- [16] N. S. Sangeetha, A. Thamizhavel, C. Tomy, S. Basu, A. M. Awasthi, P. Rajak, S. Bhattacharyya, S. Ramakrishnan, and D. Pal, Multiple charge-density-wave transitions in single-crystalline  $\text{Lu}_2\text{Ir}_3\text{Si}_5$ , *Phys. Rev. B* **91**, 205131 (2015).
- [17] Y. K. Kuo, K. M. Sivakumar, T. H. Su, and C. S. Lue, Phase transitions in  $\text{Lu}_2\text{Ir}_3\text{Si}_5$ : An experimental investigation by transport measurements, *Phys. Rev. B* **74**, 045115 (2006).
- [18] Y. Singh, D. Pal, S. Ramakrishnan, A. M. Awasthi, and S. K. Malik, Phase transitions in  $\text{Lu}_2\text{Ir}_3\text{Si}_5$ , *Phys. Rev. B* **71**, 045109 (2005).
- [19] See Supplemental Material at <http://link.aps.org/supplemental/10.1103/PhysRevB.112.224108> for details of reverse Monte Carlo and density functional theory calculations which also contains Refs. [46–51].
- [20] S. Ramakrishnan, A. Schönleber, J.-K. Bao, T. Rekiş, S. R. Kotla, A. M. Schaller, S. van Smaalen, L. Noohinejad, M. Tolkiehn, C. Paulmann, N. S. Sangeetha, D. Pal, A. Thamizhavel, and S. Ramakrishnan, Modulated crystal structure of the atypical charge density wave state of single-crystal  $\text{Lu}_2\text{Ir}_3\text{Si}_5$ , *Phys. Rev. B* **104**, 054116 (2021).
- [21] P. Juhás, T. Davis, C. L. Farrow, and S. J. L. Billinge, *PDFgetX3*: A rapid and highly automatable program for processing powder diffraction data into total scattering pair distribution functions, *J. Appl. Crystallogr.* **46**, 560 (2013).
- [22] H. P. Klug and L. E. Alexander, *X-ray Diffraction Procedures for Polycrystalline and Amorphous Materials*, edited by A. J. Edwards (Wiley, New York, 1974).
- [23] T. Egami and S. J. L. Billinge, *Underneath the Bragg Peaks: Structural Analysis of Complex Materials* (Pergamon, Oxford, England, 2003).
- [24] *Novel Application of Anomalous (Resonance) X-ray Scattering for Structural Characterization of Disordered Materials*, edited by Y. Waseda, (Springer, Berlin, Heidelberg, 1984).
- [25] V. Petkov, S. Shastri, J.-W. Kim, S. Shan, J. Luo, J. Wu, and C.-J. Zhong, Application of differential resonant high-energy X-ray diffraction to three-dimensional structure studies of nanosized materials: A case study of Pt–Pd nanoalloy catalysts, *Acta Crystallogr. Sect. A: Found. Adv.* **74**, 553 (2018).



- [26] Z. Hegedüs, T. Müller, J. Hektor, E. Larsson, T. Bäcker, S. Haas, A. L. C. Conceição, S. Gutschmidt, and U. Lienert, Imaging modalities at the Swedish Materials Science beamline at PETRA III, *IOP Conf. Ser.: Mater. Sci. Eng.* **580**, 012032 (2019).
- [27] V. Petkov, *RAD*, a program for analysis of x-ray diffraction data from amorphous materials for personal computers, *J. Appl. Crystallogr.* **22**, 387 (1989).
- [28] B. H. Toby and R. B. Von Dreele, *GSAS-II*: The genesis of a modern open-source all purpose crystallography software package, *J. Appl. Crystallogr.* **46**, 544 (2013).
- [29] C. L. Farrow, P. Juhas, J. W. Liu, D. Bryndin, E. S. Božin, J. Bloch, T. Proffen, and S. J. L. Billinge, PDFfit2 and PDFgui: Computer programs for studying nanostructure in crystals, *J. Phys.: Condens. Matter* **19**, 335219 (2007).
- [30] B. Aoun, Fullrmc, a rigid body reverse Monte Carlo modeling package enabled with machine learning and artificial intelligence, *J. Comput. Chem.* **37**, 1102 (2016).
- [31] D. A. Keen, M. G. Tucker, and M. T. Dove, Reverse Monte Carlo modelling of crystalline disorder, *J. Phys.: Condens. Matter* **17**, S15 (2005).
- [32] V. Petkov, A. Zafar, L. Gallington, S. Shastri, and B. Aoun, Structural phase diagram for Sm-substituted BiFeO<sub>3</sub> multiferroics, *Phys. Rev. Mater.* **8**, 124407 (2024).
- [33] N. P. Ong and J. W. Brill, Conductivity anisotropy and transverse magnetoresistance of NbSe<sub>3</sub>, *Phys. Rev. B* **18**, 5265 (1978).
- [34] A. LeBlanc and A. Nader, Resistivity anisotropy and charge density wave in *2H-NbSe<sub>2</sub>* and *2H-TaSe<sub>2</sub>*, *Solid State Commun.* **150**, 1346 (2010).
- [35] K. K. Kesharpu and P. D. Grigoriev, Temperature dependence of resistivity at the transition to a charge density wave state in rare-earth tritellurides, *J. Phys.: Conf. Ser.* **1238**, 012019 (2019).
- [36] H. Luo, Q. Gao, H. Liu, Y. Gu, D. Wu, C. Yi, J. Jia, S. Wu, X. Luo, Y. Xu, L. Zhao, Q. Wang, H. Mao, G. Liu, Z. Zhu, Y. Shi, K. Jiang, J. Hu, Z. Xu, and X. J. Zhou, Electronic nature of charge density wave and electron-phonon coupling in kagome superconductor KV<sub>3</sub>Sb<sub>5</sub>, *Nat. Commun.* **13**, 273 (2022).
- [37] B. Sipos, A. F. Kusmartseva, A. Akrap, H. Berger, L. Forró, and E. Tutiš, From Mott state to superconductivity in 1T-TaS<sub>2</sub>, *Nature Mater.* **7**, 960 (2008).
- [38] H. Cercellier, C. Monney, F. Clerc, C. Battaglia, L. Despont, M. G. Garnier, H. Beck, P. Aebi, L. Patthey, H. Berger, and L. Forró, Evidence for an excitonic insulator phase in 1T-TiSe<sub>2</sub>, *Phys. Rev. Lett.* **99**, 146403 (2007).
- [39] T. E. Kidd, T. Miller, M. Y. Chou, and T.-C. Chiang, Electron-hole coupling and the charge density wave transition in TiSe<sub>2</sub>, *Phys. Rev. Lett.* **88**, 226402 (2002).
- [40] S. Shimomura, C. Hayashi, G. Asaka, N. Wakabayashi, M. Mizumaki, and H. Onodera, Charge-density-wave destruction and ferromagnetic order in SmNiC<sub>2</sub>, *Phys. Rev. Lett.* **102**, 076404 (2009).
- [41] R. Gupta, A. Thamizhavel, K. P. Rajeev, and Z. Hossain, A brief review of the physical properties of charge density wave superconductor LaPt<sub>2</sub>Si<sub>2</sub>, *Supercond. Sci. Technol.* **35**, 084006 (2022).
- [42] P. M. M. Thygesen, C. A. Young, E. O. R. Beake, F. D. Romero, L. D. Connor, T. E. Proffen, A. E. Phillips, M. G. Tucker, M. A. Hayward, D. A. Keen, and A. L. Goodwin, Local structure study of the orbital order/disorder transition in LaMnO<sub>3</sub>, *Phys. Rev. B* **95**, 174107 (2017).
- [43] E. S. Bozin, W. G. Yin, R. J. Koch, M. Abeykoon, Y. S. Hor, H. Zheng, H. C. Lei, C. Petrovic, J. F. Mitchell, and S. J. L. Billinge, Local orbital degeneracy lifting as a precursor to an orbital-selective Peierls transition, *Nat. Commun.* **10**, 3638 (2019).
- [44] K. Page, M. W. Stoltzfus, Y. I. Kim, T. Proffen, P. M. Woodward, A. K. Cheetham, and R. Seshadri, Local atomic ordering in BaTaO<sub>2</sub>N studied by neutron pair distribution function analysis and density functional theory, *Chem. Mater.* **19**, 4037 (2007).
- [45] V. Petkov, J. E. Peralta, B. Aoun, and Y. Ren, Atomic structure and Mott nature of the insulating charge density wave phase of 1T-TaS<sub>2</sub>, *J. Phys.: Condens. Matter* **34**, 345401 (2022).
- [46] H. N. Nong, T. Reier, H.-S. Oh, M. Gliech, P. Paciok, T. H. T. Vu, D. Teschner, M. Heggen, V. Petkov, R. Schlögl, T. Jones, and P. Strasser, A unique oxygen ligand environment facilitates water oxidation in hole-doped IrNiO<sub>x</sub> core-shell electrocatalysts, *Nat. Catal.* **1**, 841 (2018).
- [47] P. E. Blöchl, Projector augmented-wave method, *Phys. Rev. B* **50**, 17953 (1994).
- [48] J. P. Perdew, K. Burke, and M. Ernzerhof, Generalized gradient approximation made simple, *Phys. Rev. Lett.* **77**, 3865 (1996).
- [49] G. Kresse and J. Furthmüller, Efficient iterative schemes for *ab initio* total-energy calculations using a plane-wave basis set, *Phys. Rev. B* **54**, 11169 (1996).
- [50] S. Steiner, S. Khmelevskyi, M. Marsmann, and G. Kresse, Calculation of the magnetic anisotropy with projected-augmented-wave methodology and the case study of disordered Fe<sub>1-x</sub>Co<sub>x</sub> alloys, *Phys. Rev. B* **93**, 224425 (2016).
- [51] H. Chen, Ch. D. Malliakas, A. Narayan, L. Fang, D. Y. Chung, L. K. Wagner, W.-K. Kwok, and M. G. Kanatzidis, Charge density wave and narrow energy gap at room temperature in 2D Pb<sub>3-x</sub>Sb<sub>1+x</sub>S<sub>4</sub>Te<sub>2δ</sub> with square Te sheets, *J. Am. Chem. Soc.* **139**, 11271 (2017).
- [52] A. Zafar, High Resolution x-ray diffraction data for Lu<sub>2</sub>Ir<sub>3</sub>Si<sub>5</sub>, Harvard Dataverse (2025), <https://doi.org/10.7910/DVN/IHSVLZ>.